

# Investigation of Photocatalyst Composites for Pollutant Degradation in a Microslit Reactor Utilizing High Throughput Screening Techniques

Tony B. Engelhardt, Sabine Schmitz-Stöwe, Thomas Schwarz, and Klaus Stöwe\*<sup>[a]</sup>

The high-throughput screening investigations on TiO<sub>2</sub> based photocatalyst composites presented here have been carried out in a 60-fold parallel photoreactor. Additional catalyst testing was performed in a microslit reactor system with immobilized catalysts. For further enhancing the photocatalytic activity of TiO<sub>2</sub> (P25), composites of P25 and, for example, Bi<sub>2</sub>O<sub>3</sub>, CeO<sub>2</sub>, g-C<sub>3</sub>N<sub>4</sub>, WO<sub>3</sub> or ZnO were formulated in different nominal molar ratios. The catalysts' performances were assessed by their conversion of 17 $\alpha$ -ethinyl estradiol (EE2) in aqueous solutions,

determined by LC-MS. Findings show rapid EE2 conversions in short residence times. The extensive testing of catalysts led to the conclusion that the photocatalytic conversion is rather a function of residence time than a function of the materials utilized. This makes adequate process development seem more important than material development. The novelty of this contribution lies in the unique combination of testing a wide range of composite catalysts in a unique microreactor geometry.

## Introduction


The photoexcitation of semiconducting materials and their application in photocatalysis are broadly discussed topics. Already until the end of the twentieth century, comprehensive knowledge about the photoexcitation process, the photocatalytic kinetics and their potential in chemical synthesis and environmental decontamination had been gathered.<sup>[1]</sup> Furthermore, a broad understanding about the manipulation of semiconductors in terms of doping and the additional use of co-catalysts and sensitizers was accumulated. Modern photocatalyst research investigates the behavior of semiconductor mixtures and the temporal and spatial development of heterojunctions at the materials interfaces.<sup>[2]</sup> These interfaces seem to be beneficial for exciton separation and therefore for the activity of the catalyst. Hence, the focus of this investigation lies on combinations of titanium(IV) oxide (TiO<sub>2</sub>)<sup>[3]</sup> with other semiconductors, from which bismuth(III) oxide (Bi<sub>2</sub>O<sub>3</sub>),<sup>[4–6]</sup> cerium(IV) oxide (CeO<sub>2</sub>),<sup>[7–9]</sup> iron(III) oxide (Fe<sub>2</sub>O<sub>3</sub>),<sup>[10,11]</sup> graphitic carbon nitride (g-C<sub>3</sub>N<sub>4</sub>),<sup>[12–14]</sup> niobium(V) oxide (Nb<sub>2</sub>O<sub>5</sub>),<sup>[15,16]</sup> tin(IV) oxide (SnO<sub>2</sub>),<sup>[17–20]</sup> tungsten(VI) oxide (WO<sub>3</sub>),<sup>[21–23]</sup> zinc(II) oxide (ZnO)<sup>[24–28]</sup> and zirconium(IV) oxide (ZrO<sub>2</sub>)<sup>[29–31]</sup> were


selected. In this publication, these combinations are studied following a high-throughput screening process already proposed by the authors.<sup>[32]</sup>

While a broad range of investigations on photocatalysts focusses on photocatalytic materials and their characteristics, many of these materials may not meet the requirements for an industrial application. The increased absorbance of visible light,<sup>[33]</sup> a narrowed band gap,<sup>[34]</sup> higher specific surface area<sup>[35]</sup> or even remarkable oxidation potential<sup>[36]</sup> usually do not overcome the ability of titania P25. Its low-price, industrial-scale commercial availability alongside its energy-saving UV-A absorption and activation capability in combination with photostability elevates it to its recognition as the photocatalytic standard.

Over the last thirty years of progress in photocatalysis evolution, apparently no photocatalytic investigation was transferred into an industrial application scale,<sup>[37,38]</sup> even if multiple application scenarios have been discussed and developed.<sup>[39–42]</sup> For example, the photocatalytic decontamination of waste waters may supposedly be a valuable addition to existing waste water treatment plants, but struggles with the overall minor quantum yield, slow reaction kinetics and strong mass transport limitation as well as its sensitivity to matrix composition during photocatalysis. Nevertheless, a few pilot scale approaches exist, acting towards an industrial incorporation. The deployment of sun collectors, like compound parabolic concentrators<sup>[43]</sup> in slurry type reactors<sup>[44–46]</sup> may possibly be the most energy-efficient way for catalyst activation. At the same time, these setups are strongly weather dependent. Further aspects which should be considered, are, on one hand, the separation and recycling of catalyst material, which leads to a higher complexity and susceptibility to errors of the process, and, on the other hand, mass transport limitations, which are commonly considered as negligible in well mixed up suspensions. The first two of these issues could be overcome with the application of artificial

[a] T. B. Engelhardt, Dr. S. Schmitz-Stöwe, Prof. Dr. T. Schwarz, Prof. Dr. K. Stöwe  
Institute of Chemistry  
Faculty of Natural Sciences  
University of Technology Chemnitz  
Straße der Nationen 62  
09111 Chemnitz (Germany)  
E-mail: klaus.stoewe@chemie.tu-chemnitz.de

 Supporting information for this article is available on the WWW under <https://doi.org/10.1002/open.202200180>

 © 2022 The Authors. Published by Wiley-VCH GmbH. This is an open access article under the terms of the Creative Commons Attribution Non-Commercial NoDerivs License, which permits use and distribution in any medium, provided the original work is properly cited, the use is non-commercial and no modifications or adaptations are made.

light sources and immobilized catalysts,<sup>[47,48]</sup> while mass transport limitations might become a severe issue also in this case. The overall process of transformation of a reactive species involves several different transport steps extending microkinetics into macrokinetics: the transport within the pores of the catalyst layer, the transport through a laminar fluid-dynamic boundary layer in meso- and macroscopic devices as well as the turbulent mixing in the flowing volume phase. In microstructured devices, the flow within this volume phase can be assumed as purely laminar without the existence of a boundary layer. As the slowest transport process is always rate determining, it might occur that the formation of a reactive species in the catalyst pores is faster than the transport through or into the boundary layer, thus limiting the overall reaction rate.

From this point of view, new reactor types should be considered, combining energy-saving LED technology for the activation of an immobilized, P25-based photocatalyst with a reactor geometry ensuring low mass transport limitation. The deployment of LED technology has the advantage that photocatalytic decontaminations could be realized beneath densely populated urban areas without access to sunlight. As one example from the literature,<sup>[49,50]</sup> microchannel photocatalysis reactors made of acrylate polymers were tested for their performance in dye degradation. These systems are cheap to produce, but less important for industrial incorporation, since steel exceeds the thermal and mechanical stability of polymers by far. Moreover, catalyst replacement is difficult to achieve and only low volume flows are realizable due to a lack of mechanical stability. The photocatalytic degradation of dye molecules, although easy to perform, cannot be compared to that of real contaminants with their high persistence. In contrast to these approaches, a recent publication<sup>[51]</sup> discusses a new steel-made microslit reactor for the photocatalytic mineralization of endocrine disruptive chemicals (EDC) with immobilized P25-based photocatalysts on exchangeable substrates. Utilizing this system, the present publication provides valuable contribution regarding to the photocatalytic activity of a large quantity of different catalysts. This extensive testing enabled the recognition of the reagents (EE2) conversion being a function of the residence time rather than the catalyst utilized. This is an important finding as it hints towards photocatalysis being primarily a process-specific and only secondarily a catalyst-specific property.

## Results and Discussion

### Substrate Pretreatment

With regard to the preparation process of the substrate, in which sandblasting as an integrated part of the pretreatment procedure was used to remove native oxide layers, also particles of different unalloyed black steels were accidentally processed, too. These unalloyed material particles irremovably stuck to the surface and subsequently caused spot corrosion during calcination on the stainless, highly alloyed steel substrates. As highlighted by the red circles in the ESEM image in Figure 1, IIa),

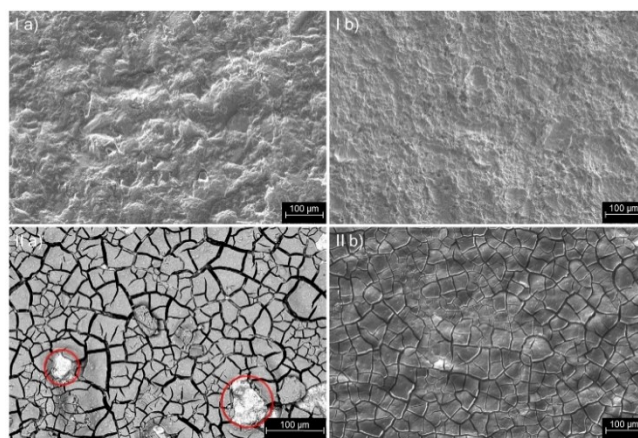


**Figure 1.** Scanning electron microscopy (ESEM) images of a rough steel substrate (I) and P25 immobilized by spray-coating on a rough steel substrate (II); comparison of corroded (a) and etched (b) surfaces after spray-coating, red circles (II a) imply accumulations of corrosion below the P25 coating; coated substrates are displayed after five experiment sets in EE2 solutions, one experiment set equals triple determination of six different modified residence times.

**Table 1.** Profilometric data of a sandblasted steel substrate (X6CrNiMo-Ti17-12-2) in different conditions: spot-corroded after sandblasting (calcination,  $\vartheta = 500\text{ }^{\circ}\text{C}$ ,  $t = 2\text{ h}$ , multiple cycles) and etched (etching:  $x(\text{HF}_{\text{aq}}) = 2\text{ vol.}\%$ ,  $x(\text{HNO}_3) = 10\text{ vol.}\%$ , ultrasonic bath,  $t = 60\text{ min}$ , passivation:  $x_{\text{citric acid}} = 4\text{ wt}\%$ );  $R_z$  – mean roughness depth;  $R_a$  – arithmetical mean roughness;  $R_t$  – total roughness.

substrate condition	$R_z/\mu\text{m}$	$R_a/\mu\text{m}$	$R_t/\mu\text{m}$
spot-corroded	$36.73 \pm 1.80$	$5.40 \pm 0.22$	$49.53 \pm 3.15$
etched	$32.89 \pm 1.77$	$4.84 \pm 0.28$	$43.33 \pm 6.94$

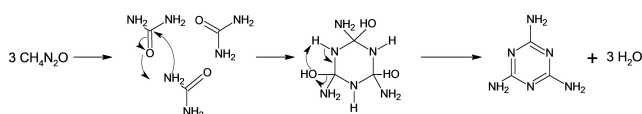
corrosion effects are obvious. This corrosion caused a lack of stability in the applied catalyst layer, with unbound P25 clods present on the catalyst surface. With an etching procedure, this spot corrosion was removed. After passivation, the chromium(III) oxide layer was restored, and thus the stainless status of the substrate. As shown in Figure 1, II b), the catalyst layer of the etched substrate showed no signs of corrosion and a dense, unaltered catalyst layer with a mud crack structure, even after multiple experimentation cycles. Profilometric measurements (Table 1) revealed that the etching process influenced all roughness variables, as a decrease was noticeable after etching, implying that the treatment smoothed out the substrate surface. Ultimately, the rough condition of the substrate was maintained. All in all, the removal of corrosion effects from the substrates surface elevated the adhesion of catalyst layers immobilized by spray-coating as a consequence of the pretreatment procedure.

## Catalyst Characterization

### *g*-C<sub>3</sub>N<sub>4</sub>

The graphitic carbon nitride used here was polymerized starting from solid urea, which forms melamine molecules via condensation reactions (Scheme 1).

Further, these fragments polymerize together with cyanamide, 2-cyanoguanidine via melon as intermediate and further on to graphitic C<sub>3</sub>N<sub>4</sub> layers under dehydration. Samples of graphitic carbon nitride as synthesized were investigated by XRD analysis and NMR spectroscopy. The powder XRD pattern, depicted in Figure 2, shows severe broadening of reflections. Since the measurement gave no distinct diffraction peaks to be



Scheme 1. Formation of melamine from urea.

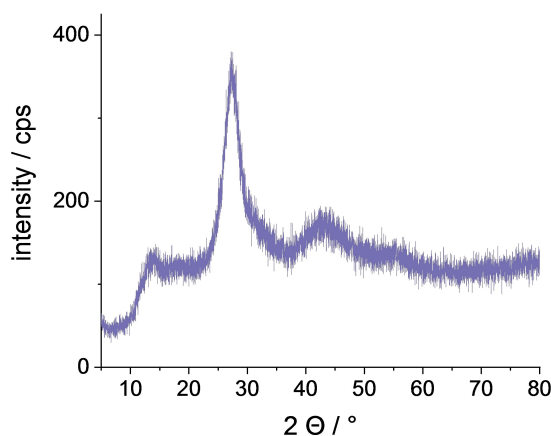


Figure 2. Powder X-ray diffraction pattern ( $\lambda(\text{CuK}\alpha_1) = 154.056 \text{ pm}$ ) of urea-derived graphitic carbon nitride (*g*-C<sub>3</sub>N<sub>4</sub>, syn.).

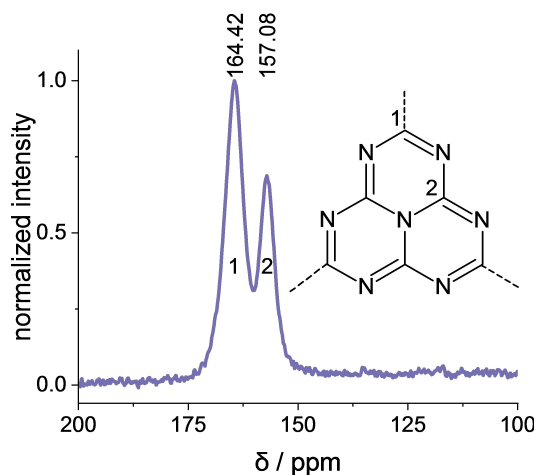


Figure 3. <sup>13</sup>C-CP-MAS NMR spectrum of urea derived graphitic carbon nitride (*g*-C<sub>3</sub>N<sub>4</sub>).

evaluated, a direct comparison to calculated values is difficult. According to the literature,<sup>[52–55]</sup> the diffraction pattern presented here still shows the presence of graphitic carbon nitride. The broad diffraction pattern visible between  $2\Theta = 12^\circ$  and  $23^\circ$  as well as high diffraction angles result from a turbostratic stacking of graphitic C<sub>3</sub>N<sub>4</sub> layers and is peaked by two broad diffraction peaks around  $2\Theta \approx 13^\circ$  and  $27.4^\circ$ . These characteristic peaks can be assigned to the in-plane (100) and interlayer-stacking (002) crystal planes of *g*-C<sub>3</sub>N<sub>4</sub> bulk agglomerates. According to the Bragg equation, the second glancing angle corresponds to an interlayer spacing of  $d = 3.35 \text{ \AA}$ , which closely resembles the values found in graphite.<sup>[56–59]</sup> Additionally, it is slightly higher than values found for *g*-C<sub>3</sub>N<sub>4</sub> in the literature.<sup>[60]</sup>

With regard to the <sup>13</sup>C-CP-MAS NMR results (Figure 3), two distinct peaks are to be identified which can be assigned to the two chemically differently surrounded carbon atoms 1 (CN<sub>2</sub>H<sub>*x*</sub>,  $\delta = 164.42 \text{ ppm}$ , still partially protonated) and 2 (CN<sub>3</sub>,  $\delta = 157.08 \text{ ppm}$ ). Consequently, the nucleus of carbon atom 2 is higher shielded than nucleus of carbon atom 1 and thus shifted downfield. As depicted in the literature, the intensity relations of both signals indicate the presence of hydrogen.<sup>[55]</sup> Since graphitic carbon nitride is a polymer, broad peaks were received in the spectrum. Concluding, both results show great resemblance to literature values,<sup>[53,55]</sup> hence it can be assumed that graphitic carbon nitride has been formed.

## Composites

Different semiconductor composites based on P25 in varying nominal molar ratios were characterized by XRD measurements (Figure 4). Diffraction patterns for comparison were derived from the International Centre for Diffraction Data (ICDD). To quantify crystal data information, Rietveld refinements of the X-ray diffraction data were performed, and for each phase, lattice parameter values for the crystalline anatase-type (space group *I*<sub>4</sub>*1*/*amd*) and rutile-type (space group *P*<sub>4</sub>*2*/*mnm*) phases *a* and *c* were determined (Supporting Information, Table S1, Figures S1–S4). Additionally, BET physisorption measurements were carried out (Supporting Information, Figures S5 and S6). Regarding the diffraction data, no other diffraction peaks than those of the binary starting materials appeared. This leads to the conclusion that no new ternary mixed metal oxide phase or superstructures due to cation ordering of the boundary phases have been formed. It appears that no detectible solid state reaction occurred during the preparation of the composites due to the chosen calcination conditions ( $\vartheta = 500^\circ\text{C}$ ,  $t = 2 \text{ h}$ ). However, the existence of *g*-C<sub>3</sub>N<sub>4</sub> (Figure 4, III), WO<sub>3</sub> (Figure 4, VI), ZnO (Figure 4, VII) and Bi<sub>2</sub>O<sub>3</sub> (Figure 4, VIII) in the mixtures is not apparent as the diffraction patterns in these systems are dominated in intensity by the titania phases. Additionally, in the case of *g*-C<sub>3</sub>N<sub>4</sub>, the broad diffraction peaks and the disordered crystal structure with a turbostratic ordering of the graphite-type layers with the overall low diffraction intensity has to be taken into account. Thus, in diffraction data of *g*-C<sub>3</sub>N<sub>4</sub>/P25 mixtures, Rietveld refinement of the diffraction pattern resulted only in crystal structure data for the titania phase. For ZnO, the

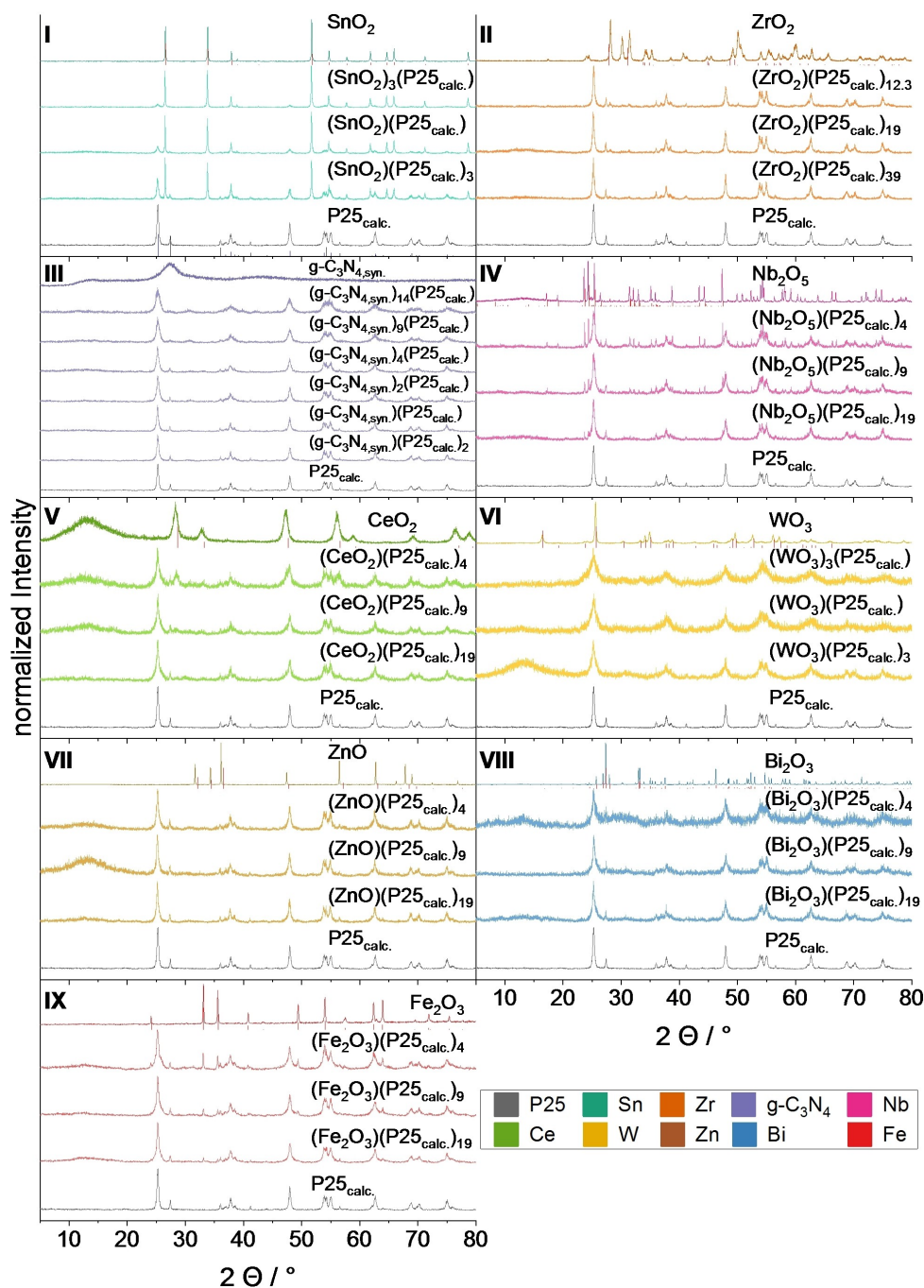


**Figure 4.** Powder X-ray diffraction (XRD) pattern of different P25-based photocatalyst composites; reference diffraction pattern are given according to ICDD: I,  $\text{TiO}_2$ , anatase,  $I4_1/amd$  (blue, ICDD 71-1166);  $\text{TiO}_2$ , rutile,  $P4_2/mnm$  (black, ICDD 71-650);  $\text{SnO}_2$ , cassiterite,  $P4_2/mnm$  (red, ICDD 72-1147); II,  $\text{ZrO}_2$ , baddeleyite,  $P2_1/c$  (red, ICDD 72-597); IV,  $\text{Nb}_2\text{O}_5$ ,  $P2$  (red, ICDD 72-1121); V,  $\text{CeO}_2$ ,  $Fm-3m$  (red, ICDD 75-76); VI,  $\text{WO}_3$ , krasnigorite,  $Pnmb$  (red, ICDD 43-679); VII,  $\text{ZnO}$ , zincite,  $P6_3mc$  (ICDD 75-1526); VIII,  $\text{Bi}_2\text{O}_3$ ,  $\alpha$ -bismuth oxide,  $P2_1/c$  (red, ICDD 71-465); IX,  $\text{Fe}_2\text{O}_3$ , hematite,  $R-3c$  (red, ICDD 72-469);  $\text{P25}_{\text{calc.}}$  – calcined P25.

mass fractions determined by refinement were lower than those given by nominal ratios, probably due to an amorphization during composite preparation, supposedly due to dissolving of  $\text{ZnO}$  in the alkaline binder (pH 7–9). In the case of the titania polymorphic forms rutile and anatase, it has to be considered that the phase ratio is influenced by the addition of the titania binder as sol (see Table S1, entries 17–19). A solid-state reaction between rutile and cassiterite-type phases in form of a mutual

cationic interdiffusion and/or defect formation is indicated by the results of lattice parameter refinements (Figure S2 Sn,R(c)), as the lattice parameter  $c$  changed significantly for the rutile type. In the case of  $\text{SnO}_2$  mixtures, no significant changes in rutile/anatase (R/A) phase ratios were found for low  $\text{SnO}_2$  amounts. Nevertheless, for high  $\text{SnO}_2$  ratios, a remarkable degradation in the R/A phase ratio is evident (compare Table S1, entry 4). In this case, all lattice parameters changed

significantly (Figure S1 Sn,A(a); Sn,A(c) and Figure S2 Sn,R(a); Sn,R(c)), but the changes in the rutile structure type are significantly higher than those of the anatase type. A marginal mutual solubility of SnO<sub>2</sub> and TiO<sub>2</sub> has already been reported in literature.<sup>[61]</sup> During the dispersion preparation of WO<sub>3</sub> and P25 in the binder, the neon yellow color of WO<sub>3</sub> vanished completely and the resulting suspension appeared colorless. Judging this perception based on the alkaline characteristics of the binder (pH 7–9), the WO<sub>3</sub> may have completely dissolved and tungstate ions might have formed instead. In all the different WO<sub>3</sub>-containing samples, the R/A ratio changed severely (compare Table S1, entry 1 with entries 14–16) while it should have stayed the same throughout the preparation process (compare the transformation temperature of metastable anatase into stable rutile,  $T = 625\text{ }^{\circ}\text{C}$ <sup>[62]</sup>).

Considering the overall appearance of the diffraction data of the WO<sub>3</sub>/P25 composites (Figure 4, VI), the solids were obtained with poor crystallinity. Thus, a quantification of phase composition via Rietveld refinements was difficult to achieve. Consequently, the data given in Table S1 (entries 14–16) should be considered with caution. Since P25 obviously lost its crystallinity just as WO<sub>3</sub> during the preparation process, the theory is that the formation of tungstate ions addressed above interacted with P25. In consequence, this leads to amorphous phases after calcination. Considering this, the alterations of lattice parameter *c* for the anatase-type phase (Figure S3, W,A(c)) are most likely coincidental. Regarding composites containing Bi<sub>2</sub>O<sub>3</sub> (Figure 4, VIII), a loss in crystallinity compared to pure P25 and  $\alpha$ -Bi<sub>2</sub>O<sub>3</sub> is obvious as well. In this case, the applied ethylene glycol in the suspension could have reduced the Bi<sub>2</sub>O<sub>3</sub> to native elemental bismuth particles early during the calcination process ( $T \approx 200\text{ }^{\circ}\text{C}$ ).<sup>[63]</sup> Those particles could be oxidized in the applied air atmosphere, consequently forming amorphous Bi<sub>2</sub>O<sub>3</sub>.<sup>[64,65]</sup> This resulted in the diminution of the Bi<sub>2</sub>O<sub>3</sub> content according to quantitative phase content determinations (Table S1, entries 20–22). Therefore, the changes in lattice parameters found by Rietveld refinement (Figure S3, Bi,A(c); Figure S4, Bi,R(a), Bi,R(c)) are most likely coincidental, too. In the cases of Nb<sub>2</sub>O<sub>5</sub>, CeO<sub>2</sub>, ZnO- and Fe<sub>2</sub>O<sub>3</sub>-containing composites, no significant lattice parameter changes were found.

Regarding BET measurements of the prepared composites, the specific surface area (SSA) is significantly increased (Figure S5) and porous composites are formed from non-porous materials (Figure S6). This phenomenon is caused by the incorporation of binder, causing a layered structure during calcination, shown in more detail in another publication.<sup>[51]</sup> Neither the SSA nor the pore volume of Nb<sub>2</sub>O<sub>5</sub> were determinable by BET measurements since nitrogen adsorbent molecules were not able to penetrate the catalyst layers. Instead, the investigations implied that the adsorbent may build up clusters at most favorable sites of a nonporous or macroporous solid according to IUPAC (type III)<sup>[66]</sup>.

## Screening Experiments in 60-fold Parallel Reactor

To acquire information about optimum ratios between pre-calcined P25 and the other semiconductors regarding their photocatalytic activity, the composite materials were prepared as mixtures with the addition of a binder. They were screened in different nominal molar ratios for EE2 decomposition. Due to low initial concentration of EE2 typically observed in waste water and high activity of the catalysts, the irradiation times were adapted to achieve conversions of around  $X_{\text{EE2}} = 0.5$ . This is necessary in order to get detectable final concentrations of EE2. Thus, this conversion can be considered as optimal for catalyst activity comparison. Due to the short irradiance times and because of the fact that the whole system was operated manually, small deviations resulted in significant absolute differences related to EE2 conversions. Consequently, the conversion results needed to be displayed in relation to the conversion realized with pure pre-calcined P25, which was measured as a standard in each screening set. This referencing procedure also allowed the comparison of different screening sets with each other. Furthermore, this representation enables the immediate recognition of whether a composite is more or less active than pre-calcined P25 alone, given by positive or negative values, as depicted in Figure 5. As the conversion of the target molecule EE2 strongly correlates with the particle size distribution during photocatalytic experiments in well-stirred suspensions, information on the particle size distribution (PSD) was additionally gathered. Small particles in the composites resulted in higher overall conversions. Results are given in Figure S7 (Supporting Information) in form of characteristic  $d_i$  values. Regarding the conversion results (Figure 5), only three catalysts ((g-C<sub>3</sub>N<sub>4</sub>,<sub>syn</sub>)(P25<sub>calc</sub>), g-C<sub>3</sub>N<sub>4</sub>,<sub>syn</sub>, and (Bi<sub>2</sub>O<sub>3</sub>)(P25<sub>calc</sub>)<sub>4</sub>) are to be considered as more active regarding the EE2 conversion than pre-calcined P25 alone. Composites containing iron oxide or tungsten oxide yielded the overall worst results. In the case of iron oxide, this may be explained by the fact that the iron oxide was adhesive to the magnetic stirring bars deployed for homogenization during the catalytic experiment. As reported in the literature, the photocatalytic performance of tungsten oxide should surpass that of P25.<sup>[23]</sup> Despite these reports, this surpassing catalytic activity could not be demonstrated in the case of EE2 conversion and P25 composites. The particle size distribution results (Figure S7) show reasonable uniformity for all composites, with the exception of composites containing g-C<sub>3</sub>N<sub>4</sub>. All in all, the particle sizes generated by the mixing of semiconductors with pre-calcined P25 resulted in larger particles than found for pre-calcined pure P25. Since the photocatalytic conversion correlates with the particle size, an “underrated” EE2 conversion for most of the catalysts compared to pre-calcined P25 could be concluded. A higher g-C<sub>3</sub>N<sub>4</sub> molar fraction is resulting in a lower average particle size. Comparing Figure 5 and Figure S7, the small particle sizes of g-C<sub>3</sub>N<sub>4</sub> could be the reason for its extraordinary conversion performance in the screening experiments. At the same time, conversion values of catalyst composites with low amounts of g-C<sub>3</sub>N<sub>4</sub> may be underrated, due to their larger particles.

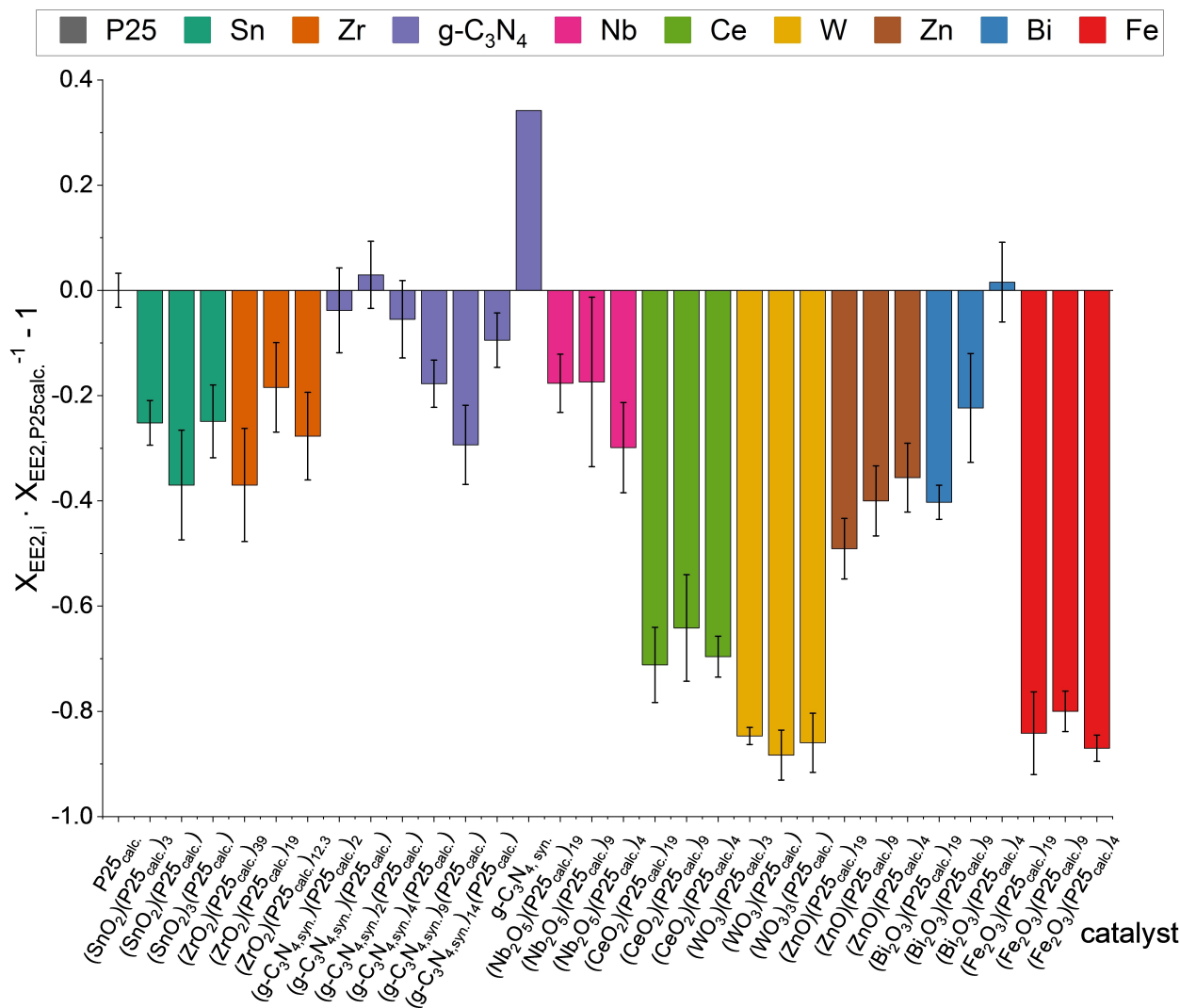


**Figure 5.** Screening of P25-based semiconductor composite photocatalysts with different molar ratios. Each value represents a separate catalytic experiment, triple conversion determination, averaged data; experiments were carried out in 60-fold parallel stirring UV–A LED photoreactor system;<sup>[32]</sup> reactant: EE2 (17 $\alpha$ -ethynyl estradiol),  $c_{\text{start}} = 15 \mu\text{g L}^{-1}$ ,  $V = 5 \text{ mL}$ ; catalysts: calcined P25 (P25<sub>calc</sub>) combined with another semiconductor in different molar ratios, calcination:  $t = 2 \text{ h}$ ,  $\vartheta = 500 \text{ }^\circ\text{C}$ ,  $m_{\text{catalyst}} = 2.5 \text{ mg}$ ; reaction:  $f_{\text{rot}} = 800 \text{ min}^{-1}$ ,  $t_{\text{dark}} = 30 \text{ min}$ ,  $t_{\text{irradiation}} = 10 \text{ s}$ ,  $E = 384 \text{ mW cm}^{-2}$ ,  $\lambda_{\text{max}} = 365 \text{ nm}$ ; EE2 content determination by UHPLC-MS/MS analysis; catalyst conversion of EE2 is given with respect to the reference compound P25 as  $X_{\text{EE2},i} \cdot X_{\text{EE2},\text{P25calc}}^{-1} - 1$ .

## Microslit Reactor Experiments

### Influence of Substrate Preparation

The influence of corrosion on the conversion of EE2 in microslit reactor experiments was investigated by testing three differently preconditioned substrates with P25 immobilized by spray-coating as the catalyst. For comparison, a non-etched and corroded (ne, c) substrate was obtained by multiple calcination cycles ( $\vartheta = 500 \text{ }^\circ\text{C}$ ,  $t = 2 \text{ h}$  for each cycle) after sandblasting. The etched (e) substrate was prepared as described in "Substrate Preparation". The results shown in Figure 6 imply that the conversion of EE2 is substantially dependent on the condition of the substrate. In the cases of the corroded (c) and non-etched (ne) specimens, an asymptotical trend to activity saturation is obvious. The etched (e) substrate provided a more linear and continuous behavior. This finding implies that the

substrate condition may influence the kinetics of the photocatalytic reaction. As literature suggests, the choice of substrate material and its pretreatment as well as the immobilization technique are significant factors in photocatalytic driven processes utilizing immobilized catalysts.<sup>[67–69]</sup> Discoveries on thin TiO<sub>2</sub> layers imply that the catalyst-substrate interaction is immanent and that the formation of oxygen vacancies on the catalysts surface is most important for photocatalytic activity. This could be enhanced by alteration of the substrate's properties.<sup>[70]</sup> For all experiments in the microslit reactor, etched substrates (e) were employed.

### Composite Investigation

Selecting the most active catalyst of each composite group on the basis of the screening experiments described in "Screening

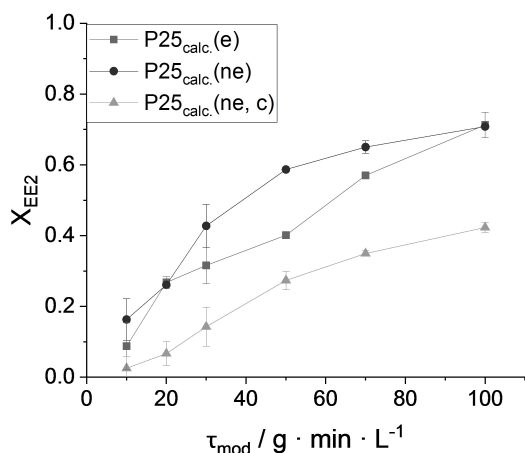


**Figure 6.** Investigation of the influence of substrate preparation on the EE2 conversion during photocatalysis, triple conversion determination, averaged data; experiments were carried out in a microslit reactor;<sup>[51]</sup> reactant: EE2 (17 $\alpha$ -ethinyl estradiol),  $c_{\text{start}} = 15 \mu\text{g L}^{-1}$ ; catalyst: P25<sub>calc.</sub>,  $m = 90 \text{ mg}$ , immobilized by spray-coating;  $c(\text{O}_2) \approx 8 \text{ mg L}^{-1}$ ; (e) – etched substrate, (ne) – non-etched substrate, (c) – corroded substrate.

Experiments in 60-fold Parallel Reactor”, additional microslit reactor experiments were carried out. Through immobilization of the composites and the addition of a binder to form rather dense layers, catalysts became more comparable, since particle size distributions were less relevant. Differences in the realized catalyst masses were inevitable since the preparation was carried out manually, but was taken into account via the application of the modified residence time  $\tau_{\text{mod}}$  (compare Equation (1), with  $Q$  – volume flow and  $m_{\text{catalyst}}$  – catalyst mass). The results are depicted in Figure 7 and show that most composites provided a smooth and uniform conversion performance. Among the others,  $(\text{WO}_3)_3(\text{P25}_{\text{calc.}})$  stood out

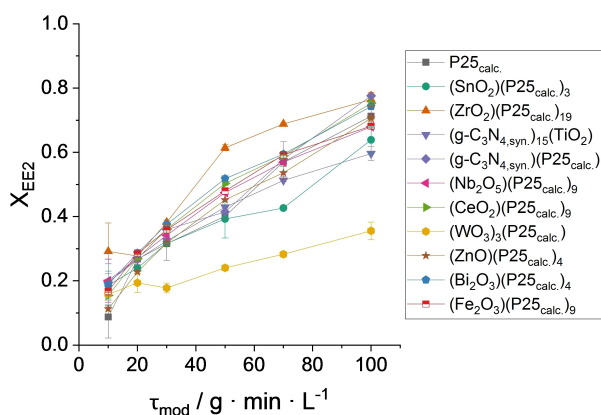


**Figure 7.** Investigation of the influence of several photocatalyst composites on the EE2 conversion, triple conversion determination, averaged data; experiments were carried out in a microslit reactor;<sup>[51]</sup> reactant: EE2 (17 $\alpha$ -ethinyl estradiol),  $c_{\text{start}} = 15 \mu\text{g L}^{-1}$ ; catalyst: P25<sub>calc.</sub>:  $m = 90 \text{ mg}$ ,  $(\text{SnO}_2)(\text{P25}_{\text{calc.}})_3$ :  $m = 110 \text{ mg}$ ,  $(\text{ZrO}_2)(\text{P25}_{\text{calc.}})_{19}$ :  $m = 90 \text{ mg}$ ,  $(\text{g-C}_3\text{N}_{4,\text{syn.}})_{15}(\text{TiO}_2)$ :  $m = 170 \text{ mg}$ ,  $(\text{g-C}_3\text{N}_{4,\text{syn.}})(\text{P25}_{\text{calc.}})$ :  $m = 80 \text{ mg}$ ,  $(\text{Nb}_2\text{O}_5)(\text{P25}_{\text{calc.}})_9$ :  $m = 90 \text{ mg}$ ,  $(\text{CeO}_2)(\text{P25}_{\text{calc.}})_9$ :  $m = 80 \text{ mg}$ ,  $(\text{WO}_3)_3(\text{P25}_{\text{calc.}})$ :  $m = 80 \text{ mg}$ ,  $(\text{ZnO})(\text{P25}_{\text{calc.}})_4$ :  $m = 80 \text{ mg}$ ,  $(\text{Bi}_2\text{O}_3)(\text{P25}_{\text{calc.}})_4$ :  $m = 80 \text{ mg}$ ,  $(\text{Fe}_2\text{O}_3)(\text{P25}_{\text{calc.}})_9$ :  $m = 100 \text{ mg}$ ; immobilized by spray-coating, differences in catalyst mass was taken into account by the application of the modified residence time  $\tau_{\text{mod}}$ ;  $c(\text{O}_2) \approx 8 \text{ mg L}^{-1}$ .

negatively with a significantly lower realized conversion overall, presumably caused by the same reasons as discussed earlier. In the case of the iron-containing composite, an elevation in conversion compared to the parallel reactor screening experiments is obvious, since adhesion to stirring bars could not cause any errors. Overall, merely one composite among all others, namely  $(\text{ZrO}_2)(\text{P25}_{\text{calc.}})_{14r}$  could be considered as superior to calcined P25 alone, since it provides significantly higher conversions at lower modified residence times ( $\tau_{\text{mod}} = 40\text{--}80 \text{ g min L}^{-1}$ ). Note that at an even higher modified residence time ( $\tau_{\text{mod}} = 100 \text{ g min L}^{-1}$ ), the composite  $(\text{g-C}_3\text{N}_{4,\text{syn.}})(\text{P25}_{\text{calc.}})$  provided significantly higher conversions than calcined pure P25. It is the only specimen which achieved this. Nevertheless, the results still may be hampered by severe mass transport limitations, as the catalyst applications in the parallel screening reactor compared to the microslit reactor are significantly different. Considering the results in the parallel screening reactor, the calcined P25 specimen should provide higher conversions compared to the other catalysts, since this is the case for most of the composites investigated during parallel reactor screening experiments. Since all composites showed almost the same activity behavior in the microslit reactor, presumably no inherent effects of the different catalyst composites – may they beneficial for conversion or not – were apparent from the data. In conclusion, EE2 conversion was exclusively a function of modified residence time and not of the composites utilized.

$$\tau_{\text{mod}} = \frac{m_{\text{catalyst}}}{Q} \quad (1)$$

#### Alternative Composite Preparation by Spray-Coating

According to the procedure described in “Immobilization”, layered semiconductor composites with a direct heterojunction by spraying of mixed suspensions were obtained. In the case of silver solution application, an indirect heterojunction by layer-by-layer spraying was achieved. While the amount of silver in the composite was well adjustable through solution concentration, the quantity of  $\text{g-C}_3\text{N}_4$  or its precursor urea, respectively, was neither adjustable nor measurable ( $m(\text{g-C}_3\text{N}_4) < 0.01 \text{ g}$ ) due to uncontrollable sublimation of urea during calcination and limits of the utilized scale (soaking into porous layer applied in the previous step). After calcination, a catalyst surface with a shiny appearance was obtained, implying that the polymer  $\text{g-C}_3\text{N}_4$  film formed indeed on the surface heterojunctions with the layer below. These immobilized catalysts were also tested in the microslit reactor system. The results are depicted in Figure 8. But again, as already discussed in the “Composite Investigation” section, the catalysts showed no significant differences in performance, presumably also due to mass transport limitations. Besides the fact that the presented modified catalyst layer preparation technique may be convenient, the method lacks controllability of the thickness of the layers produced. Additionally, in those cases in which the

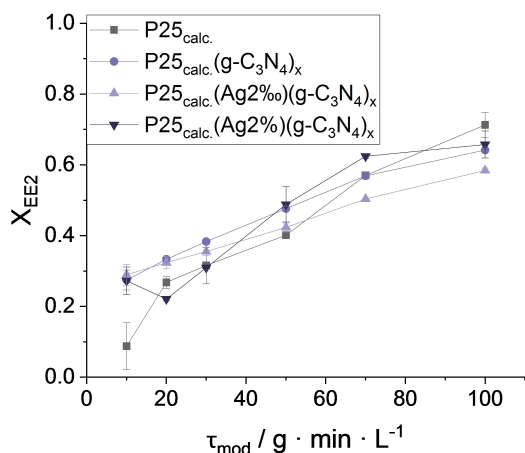


**Figure 8.** Investigation of the influence of consecutive layer application of silver nitrate and urea on a P25 layer before calcination, triple conversion determination, averaged data; experiments were carried out in a microslit reactor;<sup>[51]</sup> reactant: EE2 (17 $\alpha$ -ethinyl estradiol),  $c_{\text{start}} = 15 \mu\text{g L}^{-1}$ ; catalyst:  $m(\text{P25}_{\text{calc.}}) = 120 \text{ mg}$ , the given amount of silver illustrates its molar fraction in relation to P25, mass of g-C<sub>3</sub>N<sub>4</sub> not determinable ( $m(\text{g-C}_3\text{N}_4) < 0.01 \text{ g}$ ), immobilized by spray-coating,  $c(\text{O}_2) \approx 8 \text{ mg L}^{-1}$ .

contact area between the different components of the heterojunction and not the electron-hole separation distance is the decisive factor, a well-mixed composite might be superior compared to layered one.<sup>[71]</sup>

## Discussion

With the aim of enhancing the photocatalytic activity of P25, heterojunctions of different semiconductors, presumably beneficial for exciton separation and thus stability of the photocatalyst excited states, were investigated. Accordingly, band gap edge positions of the utilized materials were analyzed and so called type I and type II heterojunctions were found to be valuable. Therefore, specific materials were chosen according to these criteria. With regard to a future implementation in waste water cleaning, the materials utilized should be commercially available in large quantities and cheap in acquisition. Several semiconductor mixtures with P25 in different nominal molar ratios were screened regarding their performance in photocatalytic EE2 conversion in aqueous solutions in a 60-fold parallel stirring UV-A LED photoreactor setup. Subsequently, specimens that realized the highest activity among the different heterojunction photocatalyst element groups were immobilized on steel substrates by spray-coating and further tested in a bench-scale microslit reactor system with direct application relation. During screening, it was found that only few composites ((g-C<sub>3</sub>N<sub>4</sub>)<sub>syn</sub>)(P25<sub>calc.</sub>), (Bi<sub>2</sub>O<sub>3</sub>)(P25<sub>calc.</sub>)<sub>4r</sub> compare Figure 5) show small improvements regarding photocatalytic EE2 conversion. The other tested catalysts realized significantly lower conversions compared to pre-calcined pure P25. The photocatalytic properties and photostability of P25, which is itself a composite material of the two titania polymorphs anatase and rutile, alongside its cheap, commercial availability

in large quantities elevated it to the uncontested photocatalysis standard in the past that is hard to surpass. On the basis of these experiments, the beneficial characteristic of heterojunction photocatalysis on pollutant degradation stated in literature could not be reproduced. Regarding experiments in the microslit reactor, mass transport limitations became directly obvious, since the inherent differences in activity of the composites tested could not be transferred from the screening experiments onto the microslit reactor. One major difference between the two utilized systems was indeed the behavior regarding mass transport. During screening, the catalyst powders were suspended by intense stirring of the reaction mixture. Therefore, mass transport was not limited because of forced convection of all components (high dimensionless Newton and Reynolds numbers,  $Ne$  and  $Re$ , respectively). In contrast, mass transport of the reactants inside the microslit reactor in absence of a turbulent flow regime was mainly realized through diffusion. Convection only applies in the dimension parallel to the catalyst bed along flow direction. The occurrence of cross mixing is excluded at this point, since a laminar flow can be assumed. Moreover, the supply of oxygen was another severe difference between both systems. The reaction vials remained open for air exchange during screening reactions, while direct contact to air is completely excluded in the active part of the microslit reactor. With this difference in conditions taken into account, stoichiometrically consumed oxygen could not be replenished by feeding air in the microslit reactor during photocatalysis. Even if the solution was saturated with air or even pure oxygen upstream to the reactor, a critically low oxygen concentration could only be compensated by the provision of lattice oxygen by the catalyst (Mars-van-Krevelen mechanism), thus displaying a major change in reaction kinetics. This depleted lattice oxygen is only partially restorable, since a competition between different oxygen-consuming reactions occurred. In this context, formerly unpublished experiments revealed that very thick catalyst layers ( $d > 100 \mu\text{m}$ ) of P25 showed a discoloration from colorless to black during photocatalytic operation of the microslit reactor. This phenomenon was presumably based on the formation of "black titanium dioxide", which is described in the literature.<sup>[72]</sup> It relates to oxygen depletion of the titanium(IV) oxide lattice and the formation of titanium(III) species such as, for instance,  $\text{Ti}_4\text{O}_7$ , which indeed appear black in color. This is yet another indication of mass transport limitations in the microslit reactor system. This is especially relevant to the investigated EE2, since it is degraded by OH radicals in the solution film rather than in the catalyst layer, as described in a previous publication.<sup>[51]</sup> Additionally, the influence of substrate condition and preparation onto the conversion performance was investigated as well as the impact of different immobilization protocols. It was found that substrate preconditioning was essential for catalyst activity and reaction kinetics. A partially corroded substrate almost halved the conversion of EE2 compared to an etched and passivated substrate (compare Figure 6). From this finding, it cannot be ruled out that, in principle, the substrate material itself took part in the photocatalytic reaction kinetics, as electrons are formed during excitation, which may interact with the metallic substrate



material. Thus, research in this field is extremely important. With regard to the alternative catalyst layer preparation protocol, the same mass transport limitation as described just before prohibited the recognition of any differences in activity of the tested catalyst specimens (compare Figure 8). Admittedly, further investigations on this reactor type will face severe challenges, like the described mass transport limitations. Since it is very difficult to generate turbulent flow in a microstructured reactor system, the mass transport limitations need to be overcome by reduction of the diffusion length. This means, in praxis, that the microchannels need to be even thinner. At this point, a novel reactor model with an internal 3D-structuring of the catalyst layer should be considered, since lower slit heights are simply not realizable with the system described here because of sealing and other problems. Another critical point will be the scale-up of the whole process, which can be achieved only by a geometrical increase of the planar reactor area as well as an arithmetical numbering up in form of parallel reactor systems. Thus, this approach seems highly applicable for a decentralized waste water treatment units.

## Conclusion

Valuable information about the microslit reactor system and the photocatalysis research in general were gathered. It was found that mass transport limitation prohibits the occurrence of differences between the catalysts tested. Thus, the EE2 conversion appeared to be a function of residence time rather than a function of the photocatalyst utilized. In this context, an imbalance between photocatalyst material research and realization of photocatalysis application became obvious, as already stated by other authors.<sup>[73]</sup> Over fifty years of photocatalysis research with thousands of catalyst material approaches, which have not yet found industrial application, have left their marks. This research results show that it is urgently advised to accomplish an essential shift of research focus in terms of photocatalysis. More innovation in reactor and process development is imperative.

## Experimental Section

### Materials

#### Chemicals

A 17 $\alpha$ -ethinyl estradiol supply solution (EE2,  $c_{EE2}=4.5\text{ mg L}^{-1}$ , Sigma-Aldrich, Taufkirchen, Germany) was prepared by dissolution in pure water (PURELAB flex 3, ELGA LabWater Systems, Celle, Germany,  $R=18.2\text{ M}\Omega$ ,  $\text{TOC}=1\text{ ppb}$ ) for photocatalytic investigations. This stock solution was further diluted as required. For the immobilization of catalysts, P25 (nano particular  $\text{TiO}_2$ , AEROXIDE<sup>®</sup>, Evonik Industries, Mönchen-Gladbach, Germany) alongside other oxides, namely bismuth(III) oxide ( $\text{Bi}_2\text{O}_3$ , Alfa Aesar, Haverhill, Massachusetts), cerium(IV) oxide ( $\text{CeO}_2$ , Alfa Aesar, Haverhill, Massachusetts), iron(III) oxide ( $\text{Fe}_2\text{O}_3$ , Grüssing GmbH, Filsum, Germany), graphitic carbon nitride ( $\text{g-C}_3\text{N}_4$ , synthesized from urea [Grüssing GmbH, Filsum, Germany]), niobium(V) oxide ( $\text{Nb}_2\text{O}_5$ , Alfa

Aesar, Haverhill, Massachusetts), tin(IV) oxide ( $\text{SnO}_2$ , Alfa Aesar, Haverhill, Massachusetts), tungsten(VI) oxide ( $\text{WO}_3$ , VEB Laborchemie APOLDA, Apolda, Germany), zinc(II) oxide ( $\text{ZnO}$ , Thermo Fisher Scientific, Waltham, Massachusetts) and zirconium(IV) oxide ( $\text{ZrO}_2$ , Evonik Industries, Mönchen-Gladbach, Germany) were dispersed in a titania-containing sol ( $\text{TiSol-NH}_4$ , NYACOL Nano Technologies, Ashland, Massachusetts, containing 10 wt%  $\text{TiO}_2$  nanoparticles, carrier: water) which also functioned as a binder. The addition of ethylene glycol (VWR, Darmstadt, Germany, AnalaR NORMAPURE) served as a high-boiling solvent in this mixture. The impregnation of layers immobilized by spray-coating was realized with silver nitrate (Thermo Fisher, Waltham, Massachusetts) dissolved in pure water.

As mobile phases for the UHPLC-MS/MS analysis, acetonitrile (Merck, Taufkirchen, Germany, Supelco<sup>®</sup>, hyper grade for LC-MS) and pure water were deployed, both including small quantities of ammonium fluoride ( $c=0.4\text{ mg L}^{-1}$ , Merck, Taufkirchen, Germany, Supelco<sup>®</sup>, analytical grade). For the purpose of MRM (multi reaction monitoring) experiments during quantitative analyses, argon (Alphagaz, Düsseldorf, Germany, 99.9999%) was utilized as collision gas. All chemicals were employed as obtained without further purification.

### Photocatalysis Reactor Systems

Concerning high-throughput screening experiments, a self-constructed 60-fold parallel stirring UV-A LED photoreactor, already described in detail in a former publication,<sup>[32]</sup> was utilized. A novel microslit reactor system was deployed for further catalyst testing as specified in a recent publication.<sup>[51]</sup>

### Methods

#### Catalyst Preparation

For the synthesis of  $\text{g-C}_3\text{N}_4$ , an urea amount of  $m_{\text{Urea}}=10\text{ g}$  was calcined in a crucible (Carbolite, Neuhausen, Germany, AAF110,  $\vartheta=500\text{ }^\circ\text{C}$ ,  $t=2\text{ h}$ ) according to literature.<sup>[52]</sup> The residual yellow, highly brittle solid was not further purified but used as obtained. To prepare semiconductor composites of the compositions specified, calcined P25<sup>[51]</sup> was weighed out in desired amounts together with the semiconductors  $\text{Bi}_2\text{O}_3$ ,  $\text{CeO}_2$ ,  $\text{Fe}_2\text{O}_3$ ,  $\text{g-C}_3\text{N}_4$ ,  $\text{Nb}_2\text{O}_5$ ,  $\text{SnO}_2$ ,  $\text{WO}_3$ ,  $\text{ZnO}$  or  $\text{ZrO}_2$ . These solids ( $m=150\text{ mg}$ ) were thoroughly mixed in a dual asymmetric centrifuge (SpeedMixer DAC, Hauschild, Germany;  $t=24\text{ h}$ ,  $f_{\text{rot}}=300\text{ min}^{-1}$ ) with binder and ethylene glycol ( $V_{\text{binder}}=1\text{ mL}$ ,  $V_{\text{ethylene glycol}}=50\text{ }\mu\text{L}$ ), before the suspension was calcined ( $\vartheta=500\text{ }^\circ\text{C}$ ,  $t=2\text{ h}$ ). Subsequently, catalyst powders were obtained by manual grinding in an agate mortar and subsequent sieving ( $d < 100\text{ }\mu\text{m}$ ) of the resulting solids.

#### Substrate Pretreatment

Before the spray-immobilization process could be executed, the substrate surface needed to be roughened by sandblasting (quartz,  $d_{\text{avg,quartz}}=20\text{ }\mu\text{m}$ ,  $p=500\text{ kPa}$ ) to enhance the adhesion of the prepared suspensions and remove already formed oxide layers. To remove the effects of contact corrosion, the substrates were additionally etched by a stain solution ( $x(\text{HF}_{\text{aq}})=2\text{ vol}\%$ ,  $x(\text{HNO}_3)=10\text{ vol}\%$ , ultra-sonic bath,  $t=60\text{ min}$ ). Afterwards, the substrate surface was rinsed with pure water and subsequently passivated in a solution of citric acid ( $x_{\text{citric acid}}=4\text{ wt}\%$ ) to generate a fresh and passivating oxide layer. For further cleaning purposes, the substrate plates were rinsed with pure water, dried and then dipped in ethyl acetate (ultrasonic bath,  $t=15\text{ min}$ ). After drying, all leftover

organics were removed from the surface with an ozonisation technique (PSD-UV4, Novascan Technologies, Ames, Iowa,  $t = 30$  min) directly before the spray-coating process.

### Immobilization

A spray-coating technique was chosen for the preparation of immobilized catalyst layers onto a steel substrate, which is described in more detail in another publication.<sup>[51]</sup> From this procedure, catalyst layers with a thickness of approximately 10  $\mu\text{m}$  were derived. The suspensions necessary for this process were prepared as described (compare „Catalyst Preparation“ section). In the case of P25/g-C<sub>3</sub>N<sub>4</sub> composites, the application of another catalyst layer preparation workflow was investigated. It included the consecutive layer preparation of P25 followed by an optional step of silver nitrate solution impregnation in different quantities, finishing the sequence by spray-coating with urea solution. Afterwards, the calcination was performed.

### Characterization

The characterization of the crystal lattice structure parameters of powdered catalyst samples was performed with a powder X-ray diffractometer equipped with an automated, multipurpose sampler (XRD, Rigaku, Tokyo, Japan, SmartLab, Cu anode, D/tex Ultra250 detector, symmetric Johansson Ge(111) curved crystal monochromator:  $\lambda(\text{CuK}\alpha_1) = 154.056$  pm). Regarding graphitic carbon nitride, cross polarization magic angle spinning solid state nuclear magnetic resonance spectrometry (CP-MAS NMR, Bruker, Billerica, Massachusetts, Avance 400, B=9.4 T, magic angle spinning at 15 kHz in cross polarization mode, tetramethyl silane and tetrakis(trimethylsilyl)silane standards) was deployed in addition. Particle surface analysis was carried out by gas physisorption measurements and evaluated according to Brunauer–Emmett–Teller theory (BET, NOVAtouch 4LX, Quantachrome Instruments, Boynton Beach, Florida; adsorbate: nitrogen; pore size according to Dollimore–Heal). For the particle size distribution a static light scattering method (SLS, CILAS, Orléans, France 930, particle size analyzer) was used. The morphological appearance of immobilized catalyst layers were investigated by scanning electron microscopy (ESEM, Carl Zeiss Microscopy GmbH, Jena, Germany, REM Zeiss EVO15) in vacuum. Additionally, profilometric data of the uncoated substrate surface was gathered for comparison (Hommel-Etamic T8000, Jenoptik, Jena, Germany, probe type: TKU300, filter according to ISO 11562).

### Screening Experiments

For the activity screening of the catalysts, a self-constructed, 60-fold parallel stirring, UV–A LED photoreactor was utilized, as described in detail in a prior publication.<sup>[32]</sup> In contrast to the former paper, some of the screening parameters have been slightly modified from experiences made in the former investigation ( $C_{\text{EE2}} = 15 \mu\text{g L}^{-1}$ ,  $m_{\text{catalyst}} = 2.5 \text{ mg}$ ,  $t_{\text{irradiation}} = 10 \text{ s}$ ). The EE2 conversion for each sample was determined by UHPLC-MS/MS analysis.

### Microslit Reactor Experiments

All the information concerning the assembling of the microslit reactor and its operation are displayed in great detail in another publication.<sup>[51]</sup> The EE2 conversion determination was ensued by UHPLC-MS/MS analysis.

### UHPLC-MS/MS Analysis

Conversion analysis was carried out with an ultrahigh performance liquid chromatograph (UHPLC, ACQUITY UPLC H-Class, Waters Cooperation, Milford, Massachusetts) coupled to a tandem mass spectrometer (MS/MS, Xevo TQ XS, Waters Cooperation, Milford, Massachusetts), which was equipped with a patented electron spray ion source (UniSpray™, Waters Cooperation, Milford, Massachusetts). The calibration information and more details are to be found within another publication.<sup>[51]</sup>

### Acknowledgements

We cordially thank M. Sommer and A. Seifert, Professorship Polymer Chemistry at TUC, for <sup>13</sup>C-CP-MAS NMR measurements.

### Conflict of Interest

The authors declare no conflict of interest.

### Data Availability Statement

The data that support the findings of this study are available from the corresponding author upon reasonable request.

**Keywords:** 17 $\alpha$ -ethinyl estradiol · high-throughput screening · microreactors · photocatalysis · substrate conditioning

- [1] M. Anne. Fox, M. T. Dulay, *Chem. Rev.* **1993**, *93*, 341–357.
- [2] J. Low, J. Yu, M. Jaroniec, S. Wageh, A. A. Al-Ghamdi, *Adv. Mater.* **2017**, *29*, 1601694.
- [3] S. Lettieri, M. Pavone, A. Fioravanti, L. Santamaria Amato, P. Maddalena, *Materials* **2021**, *14*, 1645.
- [4] H. Rongan, L. Haijuan, L. Huimin, X. Difa, Z. Liuyang, *J. Mater. Sci. Technol.* **2020**, *52*, 145–151.
- [5] A. Rahman, Y. C. Ching, K. Y. Ching, N. Awani, A. K. Chakraborty, C. H. Chuah, N.-S. Liou, *BioResources* **2015**, *10*, 7405–7418.
- [6] Y. Liu, F. Xin, F. Wang, S. Luo, X. Yin, *J. Alloys Compd.* **2010**, *498*, 179–184.
- [7] E. Kusmirek, *Catalysts* **2020**, *10*, 1435.
- [8] B. Jiang, S. Zhang, X. Guo, B. Jin, Y. Tian, *Appl. Surf. Sci.* **2009**, *255*, 5975–5978.
- [9] M. J. Muñoz-Batista, M. N. Gómez-Cerezo, A. Kubacka, D. Tudela, M. Fernández-García, *ACS Catal.* **2014**, *4*, 63–72.
- [10] M. A. Ahmed, E. E. El-Katori, Z. H. Gharni, *J. Alloys Compd.* **2013**, *553*, 19–29.
- [11] M. Nasirian, C. F. Bustillo-Lecompte, M. Mehrvar, *J. Environ. Manage.* **2017**, *196*, 487–498.
- [12] J. Wen, J. Xie, X. Chen, X. Li, *Appl. Surf. Sci.* **2017**, *391*, 72–123.
- [13] J. Fu, J. Yu, C. Jiang, B. Cheng, *Adv. Energy Mater.* **2018**, *8*, 1701503.
- [14] S. Zhao, S. Chen, H. Yu, X. Quan, *Sep. Purif. Technol.* **2012**, *99*, 50–54.
- [15] J. Yan, G. Wu, N. Guan, L. Li, *Appl. Catal. B* **2014**, *152–153*, 280–288.
- [16] S. Furukawa, T. Shishido, K. Teramura, T. Tanaka, *ACS Catal.* **2012**, *2*, 175–179.
- [17] I. Bedja, P. V. Kamat, *J. Phys. Chem.* **1995**, *99*, 9182–9188.
- [18] S. S. Lee, H. Bai, Z. Liu, D. D. Sun, *Int. J. Hydrogen Energy* **2012**, *37*, 10575–10584.
- [19] K. Vinodgopal, P. V. Kamat, *Environ. Sci. Technol.* **1995**, *29*, 841–845.
- [20] N. Siedl, S. O. Baumann, M. J. Elser, O. Diwald, *J. Phys. Chem. C* **2012**, *116*, 22967–22973.
- [21] K. K. Akurati, A. Vital, J.-P. Dellemann, K. Michalow, T. Graule, D. Ferri, A. Baiker, *Appl. Catal. B* **2008**, *79*, 53–62.

- [22] J. He, Q. Luo, Q. Z. Cai, X. W. Li, D. Q. Zhang, *Mater. Chem. Phys.* **2011**, *129*, 242–248.
- [23] O. Arutanti, A. B. D. Nandiyanto, T. Ogi, F. Iskandar, T. O. Kim, K. Okuyama, *J. Alloys Compd.* **2014**, *591*, 121–126.
- [24] S. Janitabar-Darzi, A. R. Mahjoub, *J. Alloys Compd.* **2009**, *486*, 805–808.
- [25] X. Liu, L. Pan, T. Lv, Z. Sun, *J. Colloid Interface Sci.* **2013**, *394*, 441–444.
- [26] G. Yang, Z. Yan, T. Xiao, *Appl. Surf. Sci.* **2012**, *258*, 8704–8712.
- [27] D. Ramírez-Ortega, A. M. Meléndez, P. Acevedo-Peña, I. González, R. Arroyo, *Electrochim. Acta* **2014**, *140*, 541–549.
- [28] B. Pant, G. P. Ojha, Y.-S. Kuk, O. H. Kwon, Y. W. Park, M. Park, *Nanomaterials* **2020**, *10*, 1960.
- [29] J. Tian, Q. Shao, J. Zhao, D. Pan, M. Dong, C. Jia, T. Ding, T. Wu, Z. Guo, *J. Colloid Interface Sci.* **2019**, *541*, 18–29.
- [30] B. M. Pirezada, N. A. Mir, N. Qutub, O. Mehraj, S. Sabir, M. Muneer, *Mater. Sci. Eng. B* **2015**, *193*, 137–145.
- [31] S. Ramamoorthy, S. Das, R. Balan, I. C. Lekshmi, *Mater. Today: Proc.* **2021**, *47*, 4641–4646.
- [32] T. B. Engelhardt, S. Schmitz-Stöwe, T. Schwarz, K. Stöwe, *Materials* **2020**, *13*, 1365.
- [33] M. A. Nasalevich, M. G. Goesten, T. J. Savenije, F. Kapteijn, J. Gascon, *Chem. Commun.* **2013**, *49*, 10575–10577.
- [34] E. M. Samsudin, S. B. Abd Hamid, *Appl. Surf. Sci.* **2017**, *391*, 326–336.
- [35] Y. Wen, M. Feng, P. Zhang, H.-C. Zhou, V. K. Sharma, X. Ma, *ACS ES&T Eng.* **2021**, *1*, 804–826.
- [36] E. Speckmeier, T. G. Fischer, K. Zeitler, *J. Am. Chem. Soc.* **2018**, *140*, 15353–15365.
- [37] M. J. Muñoz-Batista, A. N. Muñoz, R. Luque, *Heterogeneous Photocatalysis: Recent Advances*, Springer, Berlin, **2020**.
- [38] L. Candish, K. D. Collins, G. C. Cook, J. J. Douglas, A. Gómez-Suárez, A. Jolitt, S. Keess, *Chem. Rev.* **2022**, *122*, 2907–2980.
- [39] J. J. Rueda-Marquez, I. Levchuk, P. Fernández Ibañez, M. Sillanpää, *J. Cleaner Prod.* **2020**, *258*, 120694.
- [40] S. Ya. Kuchmiy, *Theor. Exp. Chem.* **2021**, *57*, 237–261.
- [41] K. H. Ng, S. Y. Lai, C. K. Cheng, Y. W. Cheng, C. C. Chong, *Chem. Eng. J.* **2021**, *417*, 128847.
- [42] W. Zhang, A. R. Mohamed, W. Ong, *Angew. Chem. Int. Ed.* **2020**, *59*, 22894–22915; *Angew. Chem.* **2020**, *132*, 23092–23115.
- [43] C. Jiang, L. Yu, S. Yang, K. Li, J. Wang, P. D. Lund, Y. Zhang, *Energies* **2020**, *13*, 695.
- [44] J. J. Murcia Mesa, J. S. Hernández Niño, W. González, H. Rojas, M. C. Hidalgo, J. A. Navio, *Water* **2021**, *13*, 2705.
- [45] J. Colina-Márquez, F. Machuca-Martínez, G. Li Puma, *Environ. Sci. Technol.* **2009**, *43*, 8953–8960.
- [46] S. Malato, J. Blanco, A. Vidal, C. Richter, *Appl. Catal. B* **2002**, *37*, 1–15.
- [47] S. Moles, R. Mosteo, J. Gómez, J. Szpunar, S. Gozzo, J. R. Castillo, M. P. Ormad, *Water* **2020**, *12*, 1453.
- [48] A. K. Ray, A. A. C. M. Beenackers, *AIChE J.* **1998**, *44*, 477–483.
- [49] A. Baruah, A. Singh, V. Sheoran, B. Prakash, A. K. Ganguli, *Mater. Res. Express* **2018**, *5*, 075019.
- [50] V. Katoch, N. Sharma, M. Sharma, M. Baghoria, J. J. Panda, M. Singh, B. Prakash, *Environ. Sci. Pollut. Res. Int.* **2021**, *28*, 19155–19165.
- [51] T. B. Engelhardt, M. Zhu, C. Heilmann, S. Schmitz-Stöwe, T. Schwarz, K. Stöwe, *Catalysts* **2021**, *11*, 1351.
- [52] F. Dong, L. Wu, Y. Sun, M. Fu, Z. Wu, S. C. Lee, *J. Mater. Chem.* **2011**, *21*, 15171.
- [53] B. V. Lotsch, M. Döblinger, J. Sehnert, L. Seyfarth, J. Senker, O. Oeckler, W. Schnick, *Chem. Eur. J.* **2007**, *13*, 4969–4980.
- [54] J. Gao, Y. Zhou, Z. Li, S. Yan, N. Wang, Z. Zou, *Nanoscale* **2012**, *4*, 3687.
- [55] W. Li, Z. Guo, L. Jiang, L. Zhong, G. Li, J. Zhang, K. Fan, S. Gonzalez-Cortes, K. Jin, C. Xu, T. Xiao, P. P. Edwards, *Chem. Sci.* **2020**, *11*, 2716–2728.
- [56] J. Y. Howe, C. J. Rawn, L. E. Jones, H. Ow, *Powder Diffr.* **2003**, *18*, 150–154.
- [57] R. S. Aga, C. L. Fu, M. Krčmar, J. R. Morris, *Phys. Rev. B* **2007**, *76*, 165404.
- [58] P. L. Walker, H. A. McKinstry, C. C. Wright, *Ind. Eng. Chem.* **1953**, *45*, 1711–1715.
- [59] W. Ruland, B. Smarsly, *J. Appl. Crystallogr.* **2002**, *35*, 624–633.
- [60] A. Thomas, A. Fischer, F. Goettmann, M. Antonietti, J.-O. Müller, R. Schlögl, J. M. Carlsson, *J. Mater. Chem.* **2008**, *18*, 4893.
- [61] Y. Xie, S. Yin, H. Yamane, T. Hashimoto, H. Machida, T. Sato, *Chem. Mater.* **2008**, *20*, 4931–4935.
- [62] J. L. Murray, H. A. Wriedt, *J. Phase Equilibria* **1987**, *8*, 148–165.
- [63] X. Liu, J. Zeng, S. Zhang, R. Zheng, X. Liu, Y. Qian, *Chem. Phys. Lett.* **2003**, *374*, 348–352.
- [64] C.-C. Huang, T.-Y. Wen, K.-Z. Fung, *Mater. Res. Bull.* **2006**, *41*, 110–118.
- [65] J. Xia, M. Tang, C. Chen, S. Jin, Y. Chen, *Trans. Nonferrous Met. Soc. China* **2012**, *22*, 2289–2294.
- [66] M. Thommes, K. Kaneko, A. V. Neimark, J. P. Olivier, F. Rodriguez-Reinos, J. Rouquerol, K. S. W. Sing, *Pure Appl. Chem.* **2015**, *87*, 1051–1069.
- [67] L. Lopez, W. A. Daoud, D. Dutta, B. C. Panther, T. W. Turney, *Appl. Surf. Sci.* **2013**, *265*, 162–168.
- [68] V. Porley, N. Robertson, in *Nanostructured Photocatalysts* (Eds. R. Boukherroub, S. B. Ogale, N. Robertson), Elsevier, **2020**, pp. 129–171.
- [69] S. Ortelli, M. Blosi, S. Albonetti, A. Vaccari, M. Dondi, A. L. Costa, *J. Photochem. Photobiol. Chem.* **2014**, *276*, 58–64.
- [70] D. Kazazis, S. Guha, N. A. Bojarczuk, A. Zaslavsky, H.-C. Kim, *Appl. Phys. Lett.* **2009**, *95*, 064103.
- [71] N. Siedl, S. O. Baumann, M. J. Elser, O. Diwald, *J. Phys. Chem. C* **2012**, *116*, 22967–22973.
- [72] X. Chen, L. Liu, F. Huang, *Chem. Soc. Rev.* **2015**, *44*, 1861–1885.
- [73] S. K. Loeb, P. J. J. Alvarez, J. A. Brame, E. L. Cates, W. Choi, J. Crittenden, D. D. Dionysiou, Q. Li, G. Li-Puma, X. Quan, D. L. Sedlak, T. David Waite, P. Westerhoff, J.-H. Kim, *Environ. Sci. Technol.* **2019**, *53*, 2937–2947.

Manuscript received: August 10, 2022  
Revised manuscript received: October 4, 2022